Eur. J. Mech. B/Fluids 18 (1999) 1067–1084
© 1999 Éditions scientifiques et médicales Elsevier SAS. All rights reserved

Inviscid evolution of incompressible swirling flows in pipes: The dependence of the flow structure upon the inlet velocity field

J. Ortega-Casanova *, R. Fernández-Feria

Universidad de Málaga, E.T.S. Ingenieros Industriales, 29013 Málaga, Spain

(Received 22 May 1998; revised 11 May 1999; accepted 15 August 1999)

Abstract – This paper analyses the influence of the inlet swirl on the structure of incompressible inviscid flows in pipes. To that end, the inviscid evolution along a pipe of varying radius with a central body situated inside the pipe is studied for three different inlet swirling flows by solving the Bragg–Hawthorne equation both asymptotically and numerically. The downstream structure of the flow changes abruptly above certain threshold values of the swirl parameter (L). In particular, there exist a value L_r above which a near-wall region of flow reversal is formed downstream, and a critical value L_f above which the axial vortex flow breaks down. It is shown that the dependence upon the pipe geometry of these critical values of the swirl parameter varies strongly with the inlet azimuthal velocity profile considered. An excellent agreement between asymptotic and numerical results is found. © 1999 Éditions scientifiques et médicales Elsevier SAS

incompressible swirling flows / Bragg–Hawthorne equation

1. Introduction

The breakdown of swirling flows is a phenomenon of technological and theoretical fluid dynamic interest (see, e.g. Delery [1] for a review). A frequent and relatively simple tool to analyse it has been the study of swirling flows in pipes, both experimentally (e.g. Sarpkaya [2]) and numerically (e.g. Beran and Culik [3]). In particular, a number of theoretical and numerical works have made use of the inviscid flow equations to explain vortex breakdown in pipes (e.g. Stuart [4], Buntine and Saffman [5] and Wang and Rusak [6]). This inviscid flow approach has the advantage of its simplicity, because the axisymmetric swirling flow is governed by a single partial differential equation whose structure depends on the initial or inlet swirling flow considered. Different inlet flows have been used in the literature, most of them showing the phenomenon of vortex breakdown downstream in the pipe when the intensity of the inlet swirl, measured by a swirl parameter, is above a certain threshold value which depends on the inlet flow itself and on the pipe geometry. The inlet swirling flows used in previous works usually consisted of a Rankine, or a Gaussian-like (Burgers'), vortex combined with an uniform axial velocity. In fact, the selection of the inlet flow is independent of the inviscid assumptions and somewhat ambiguous, because any velocity field with cylindrical symmetry is a solution to the incompressible cylindrical Euler equations governing the far upstream flow. Thus, although the equations governing the flow inside the pipe are non-viscous, they contain information on the inlet velocity profile, which in most of the cases considered (e.g. Burgers' vortex) needs the previous action of viscosity to develop. Therefore, it is not completely clear whether the downstream structure of the flow, and in particular the breakdown of the vortex core, is a purely inviscid phenomenon practically independent of the inlet flow considered, or it is a consequence of the indirect action of viscosity through the inlet conditions. To shed some light on this subject, this paper

* Correspondence and reprints; jortega@uma.es

considers a pipe with a central body situated inside, an element present upstream in most swirl generators, being the device responsible for the intense axial swirling jet inside the downstream section of the pipe. We consider three different possibilities for the velocity profiles far upstream of the central body base, and look for the corresponding inviscid solutions downstream. Thus, the velocity profiles at the pipe inlet just after the central body base are genuine 'inviscid' velocity profiles, corresponding to three different physical upstream conditions of the flow. The asymptotic solution of the inviscid equations far downstream in the pipe shows that the flow structures in the three cases considered are not just quantitatively, but also qualitatively very different. Numerical integration of the inviscid flow equations corroborates these asymptotic results.

2. Formulation of the problem

Under the assumptions of incompressible, axisymmetric and steady flow of an inviscid fluid with velocity field (u, v, w) in cylindrical polar co-ordinates (r, θ, z), the stream function Ψ of the meridional motion,

$$u = -\frac{1}{r}\frac{\partial \Psi}{\partial z}, \qquad w = \frac{1}{r}\frac{\partial \Psi}{\partial r}, \tag{1}$$

satisfies the Bragg–Hawthorne [7] equation (also called Squire–Long equation; hereafter referred to as B–H equation),

$$\frac{\partial^2 \Psi}{\partial z^2} - \frac{1}{r}\frac{\partial \Psi}{\partial r} + \frac{\partial^2 \Psi}{\partial r^2} = r^2 \frac{dH}{d\Psi} - C\frac{dC}{d\Psi}, \tag{2}$$

where $H(\Psi)$ and $C(\Psi)$ are the Bernoulli function and the circulation, respectively,

$$H = \frac{p}{\rho} + \frac{1}{2}(u^2 + v^2 + w^2), \qquad C = rv, \tag{3}$$

with p the pressure field and ρ the constant fluid density. We are interested here in solving this equation inside a pipe with the form given in *figure 1*, with a wall contraction and a central body located inside. The inner wall ends at $z = 0$, and its non-dimensional radius is given by (see *figure 1*):

$$\eta_i(\xi) \equiv \frac{r_i(z)}{r_2} = R \tanh(-\alpha\xi) \quad \text{for } -\xi_1 \leqslant \xi \leqslant 0, \tag{4}$$

$$\eta_i(\xi) = 0 \quad \text{for } 0 < \xi \leqslant \xi_2. \tag{5}$$

Here we have used the pipe inlet radius r_2 as the characteristic length, defining

$$\eta \equiv \frac{r}{r_2}, \qquad \xi \equiv \frac{z}{r_2}, \qquad R \equiv \frac{r_1}{r_2}, \tag{6}$$

where r_1 is the upstream radius of the central body, which axial length is characterized by the geometric factor α (see *figure 1*). The radius of the outer wall, $r_o(z)$, is defined in terms of r_i and the given interior section $A(z)$ of the pipe:

$$\eta_o(\xi) \equiv \frac{r_o(z)}{r_2} = \sqrt{\mathcal{S}(\xi) + \eta_i^2(\xi)}, \quad \mathcal{S}(\xi) \equiv \frac{A(z)}{\pi r_2^2}. \tag{7}$$

The particular forms of $\mathcal{S}(\xi)$ used in the numerical computations will be specified below in Section 4.

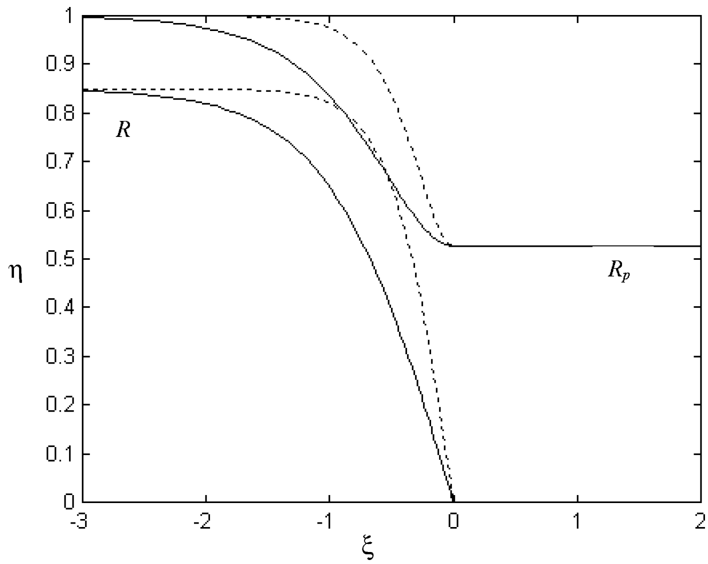

Figure 1. Pipe geometry for $\alpha = 1$ (continuous lines) and $\alpha = 2$ (dotted lines) for $R = 0.85$. Although the domain shown is $-3 \leqslant \xi \leqslant 2$, in all the numerical computations of Section 4 we used $-10 \leqslant \xi \leqslant 10$ (i.e. $\xi_1 = \xi_2 = 10$).

The functions $H(\Psi)$ and $C(\Psi)$ are obtained from the velocity profiles at the pipe inlet, $\xi = -\xi_1$, $R \leqslant \eta \leqslant 1$, which are characterized by an axial velocity U and an angular velocity Ω. These parameters are used to define the non-dimensional velocity components as

$$\overline{u} \equiv \frac{u}{U}, \qquad \overline{v} \equiv \frac{v}{\Omega r_2}, \qquad \overline{w} \equiv \frac{w}{U}, \tag{8}$$

and a swirl parameter

$$L \equiv \frac{\Omega r_2}{U}. \tag{9}$$

We shall use three different inlet velocity profiles, denoted by (a), (b) and (c) in what follows:

$$\text{(a)} \quad \overline{u} = 0, \quad \overline{v} = \eta, \quad \overline{w} = 1, \tag{10}$$

$$\text{(b)} \quad \overline{u} = 0, \quad \overline{v} = \frac{\eta^2 - R^2}{\eta(1 - R^2)}, \quad \overline{w} = 1, \tag{11}$$

$$\text{(c)} \quad \overline{u} = 0, \quad \overline{v} = \frac{R^2(1 - \eta^2)}{\eta(1 - R^2)}, \quad \overline{w} = 1, \tag{12}$$

where $\eta \in [R, 1]$. All of them correspond to a cylindrical ($u = 0$) flow with an uniform axial velocity ($w = U$). In relation to the azimuthal velocity, the first profile corresponds to a rigid body rotation in between the two pipe walls, both rotating with an angular velocity Ω; the second one corresponds to a rotation of the outer wall, with the inner wall at rest, and the third one to a rotation of the inner wall only. These three different inlet azimuthal profiles are plotted in *figure 2*. The corresponding pressure (given by the radial momentum balance, $\rho v^2/r = \partial p/\partial r$) and vorticity ($\boldsymbol{\omega} = (\gamma, \zeta, \chi) = ((1/r)\partial w/\partial\theta - \partial v/\partial z, \partial u/\partial z - \partial w/\partial r, (1/r)\partial(rv)/\partial r - (1/r)\partial u/\partial\theta)$) distributions at the pipe inlet are:

$$\text{(a)} \quad \overline{p} = \frac{1}{2}\eta^2 + \overline{p_0}, \quad \overline{\gamma} = 0, \quad \overline{\zeta} = 0, \quad \overline{\chi} = 2, \tag{13}$$

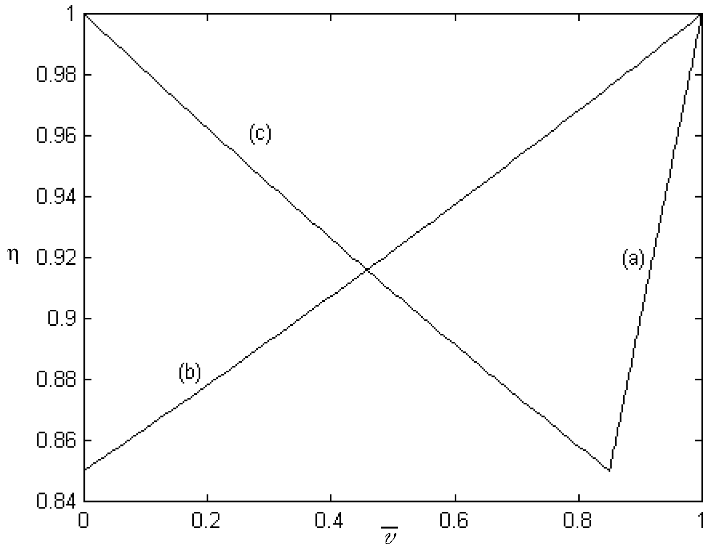

Figure 2. Profiles of the inlet azimuthal velocity for the three cases and $R = 0.85$.

$$\text{(b)}\quad \overline{p} = \frac{1}{(1-R^2)^2}\left(\frac{\eta^2}{2} - \frac{R^4}{2\eta^2} - 2R^2\ln\eta\right) + \overline{p_0}, \quad \overline{\gamma} = 0, \quad \overline{\zeta} = 0, \quad \overline{\chi} = \frac{\eta^2 - R^2}{\eta(1-R^2)}, \tag{14}$$

$$\text{(c)}\quad \overline{p} = \frac{R^4}{(1-R^2)^2}\left(\frac{\eta^2}{2} - \frac{1}{2\eta^2} - 2\ln\eta\right) + \overline{p_0}, \quad \overline{\gamma} = 0, \quad \overline{\zeta} = 0, \quad \overline{\chi} = -\frac{2R^2}{1-R^2}, \tag{15}$$

where the non-dimensional pressure and vorticity have been defined as

$$\overline{p} \equiv \frac{p}{\rho(\Omega r_2)^2}, \qquad \overline{\boldsymbol{\omega}} \equiv \frac{\boldsymbol{\omega}}{\Omega}, \tag{16}$$

and $\overline{p_0}$ is a reference value, different for each of the three cases (for instance, $\overline{p_0} = \overline{p}(\eta = 0)$ for the case (a), $\overline{p_0} = \overline{p}(\eta = 1)$ for the case (c), and $\overline{p_0}$ depends on R for the case (b)).

In non-dimensional form, the B–H equation (2) may be written as

$$\psi_{\xi\xi} - \frac{1}{\eta}\psi_\eta + \psi_{\eta\eta} = 4L^2\left(\eta^2\frac{d\overline{H}}{d\psi} - \overline{C}\frac{d\overline{C}}{d\psi}\right), \tag{17}$$

where subscripts indicate differentiation and

$$\psi \equiv \frac{\Psi}{(1/2)Ur_2^2}, \qquad \overline{H} \equiv \frac{H}{\Omega^2 r_2^2}, \qquad \overline{C} \equiv \frac{C}{\Omega r_2^2}. \tag{18}$$

$\overline{H}$ and $\overline{C}$ are obtained from (10)–(15):

$$\text{(a)}\quad \overline{H}(\psi) = \psi, \quad \overline{C}(\psi) = \psi + R^2, \tag{19}$$

$$\text{(b)}\quad \overline{H}(\psi) = \frac{1}{(1-R^2)^2}\left(\psi - R^2\ln\left(\psi + R^2\right)\right), \quad \overline{C}(\psi) = \frac{\psi}{1-R^2}, \tag{20}$$

$$\text{(c)}\quad \overline{H}(\psi) = \frac{R^4}{(1-R^2)^2}\left(\psi - \ln\left(\psi + R^2\right)\right), \quad \overline{C}(\psi) = R^2\left(1 - \frac{\psi}{1-R^2}\right), \tag{21}$$

where an irrelevant additive constant in $\overline{H}$ has been omitted. The B–H equation (17) can be written in a compact form for the three inlet flow considered as

$$\psi_{\xi\xi} - \frac{1}{\eta}\psi_\eta + \psi_{\eta\eta} = a^2\left(c_1\eta^2 - \psi + c_2 + \eta^2\frac{c_3\psi + c_4}{\psi + R^2}\right), \tag{22}$$

where the constants a, and $c_i,\ i = 1, 2, 3, 4,$ are given by

$$\text{(a)}\quad c_1 = 1,\quad c_2 = -R^2,\quad c_3 = 0,\quad c_4 = 0,\quad a = 2L, \tag{23}$$

$$\text{(b)}\quad c_1 = 0,\quad c_2 = 0,\quad c_3 = 1,\quad c_4 = 0,\quad a = \frac{2L}{1 - R^2}, \tag{24}$$

$$\text{(c)}\quad c_1 = 1,\quad c_2 = 1 - R^2,\quad c_3 = 0,\quad c_4 = -1,\quad a = \frac{2LR^2}{1 - R^2}. \tag{25}$$

Note that the resulting B–H equation is linear only for the inlet flow corresponding to the case (a); for the cases (b) and (c) the equation is non-linear. This equations must be solved with boundary conditions on the four boundaries. At the inlet ($\xi = -\xi_1$), the radial distributions of ψ is given by the uniform axial velocity profile considered in all three cases and fixing ψ on the inner wall equal to zero ($\psi(\eta = R) = 0$). The wall of the central body base and the axis of symmetry ($\eta = \eta_i$) are streamlines, and so is the wall of the outer wall ($\eta = \eta_o$). There, the streamfunction is constant and equal to its value at the inlet. Finally, the flow is considered cylindrical at the pipe outlet ($\xi = \xi_2$). One may impose, for instance, that the radial velocity vanishes at the pipe outlet ($\overline{u}(\xi = \xi_2) = 0$). However, this condition is too restrictive, and we have used the weaker condition that the axial gradient of the radial velocity vanishes, $\overline{u}_\xi = \psi_{\xi\xi} = 0$ at $\xi = \xi_2$ (see Buntine and Saffman [5], for a discussion of these and other possible boundary conditions at the pipe outlet). In summary, the four boundary conditions are:

$$\psi(\eta, \xi = -\xi_1) = \eta^2 - R^2,\quad R \leqslant \eta \leqslant 1, \tag{26}$$

$$\psi(\eta = \eta_i, \xi) = 0,\quad -\xi_1 \leqslant \xi \leqslant \xi_2, \tag{27}$$

$$\psi(\eta = \eta_o, \xi) = 1 - R^2,\quad -\xi_1 \leqslant \xi \leqslant \xi_2, \tag{28}$$

$$\psi_{\xi\xi} = 0,\quad \xi = \xi_2,\ 0 \leqslant \eta \leqslant R_p, \tag{29}$$

where

$$R_p = \frac{r_3}{r_2}, \tag{30}$$

and r_3 is the outlet radius of the pipe.

3. Downstream asymptotic solution and critical values of the swirl parameter

In this section we look for cylindrical solutions of (22) in the far downstream region ($\xi \gg 1$), where $\eta_i = 0$ and $\eta_o \to R_p$, corresponding to the three inlet cylindrical flows (10), (11) and (12). We shall see that these solutions provide critical values of L above which the flow structure changes abruptly.

In order to linearize the equation for the cases (b) and (c), we further assume that R_p is small. Thus, far downstream, both η and ψ are small, and the non-linear term in the right-hand side of (22) can be linearized to

$$\eta^2\frac{c_3\psi + c_4}{\psi + R^2} = \frac{c_4\eta^2}{R^2} + \eta^2\psi\left(\frac{c_3}{R^2} - \frac{c_4}{R^4}\right) + \mathrm{O}(\eta^2\psi^2). \tag{31}$$

Retaining terms up to $O(\eta^2)$ (and, therefore, with errors $O(\eta^2\psi) = O(R_p^2(1-R^2))$; note that for a constant fluid section, $\mathcal{S} = \text{constant} = 1 - R^2 = R_p^2$, the errors are $O(R_p^4)$), equation (22) becomes

$$\psi_{\xi\xi} - \frac{1}{\eta}\psi_\eta + \psi_{\eta\eta} = a^2\left(c_1\eta^2 - \psi + c_2 + c_4\frac{\eta^2}{R^2}\right). \tag{32}$$

It must be noted that this equation is exact for the case (a), where $c_3 = c_4 = 0$. Defining

$$F \equiv \psi - c_2 - \eta^2\left(c_1 + \frac{c_4}{R^2}\right), \tag{33}$$

equation (32), and the boundary conditions on $\eta = \eta_i = 0$ and $\eta = \eta_o \to R_p$, (27)–(29) become

$$F_{\xi\xi} - \frac{1}{\eta}F_\eta + F_{\eta\eta} + a^2 F = 0, \tag{34}$$

$$F = -c_2 - \eta^2\left(c_1 + \frac{c_4}{R^2}\right), \quad \eta = 0,\ -\xi_1 \leqslant \xi \leqslant \xi_2, \tag{35}$$

$$F = 1 - R^2 - c_2 - \eta^2\left(c_1 + \frac{c_4}{R^2}\right), \quad \eta = R_p,\ -\xi_1 \leqslant \xi \leqslant \xi_2. \tag{36}$$

Thus, in this limit of large ξ, the problem can be solved separating variables, $F(\xi,\eta) = X(\xi)Q(\eta)$. Substituting into (34) with (35)–(36) one has a two-point boundary problem for $Q(\eta)$, which yields the following solution as an eigenexpansion in Bessel functions of the first order J_1 (first kind) and Y_1 (second kind):

$$F = \eta\left[A_0 J_1(a\eta) + B_0 Y_1(a\eta)\right] + \sum_{n=1}^{\infty}\left(C_n e^{\lambda_n\xi} + D_n e^{-\lambda_n\xi}\right)\eta J_1\left(\frac{j_{1,n}}{R_p}\eta\right), \tag{37}$$

where $j_{1,n}$ is the nth zero of J_1 (see, e.g., Abramowitz and Stegun [8]), and the eigenvalues λ_n are given by

$$\lambda_n = \sqrt{\frac{j_{1,n}^2}{R_p^2} - a^2}. \tag{38}$$

Constants B_0 and A_0 are

$$\text{(a)}\quad B_0 = -R^2 L\pi, \quad A_0 = \frac{1 - R_p^2 - B_0 R_p Y_1(2LR_p)}{R_p J_1(2LR_p)}, \tag{39}$$

$$\text{(b)}\quad B_0 = 0, \quad A_0 = \frac{1 - R^2}{R_p J_1(aR_p)}, \tag{40}$$

$$\text{(c)}\quad B_0 = \frac{(1 - R^2)\pi a}{2}, \quad A_0 = \frac{(1 - R^2)R_p - R^2 B_0 Y_1(aR_p)}{R^2 J_1(aR_p)}. \tag{41}$$

All the constants C_n in (37) should be zero, and the constants D_n cannot be determined within the present asymptotic limit of large ξ; they are, however, irrelevant for $\xi \gg 1$, where only the first two terms in (37) are important.

It is interesting to compare the three different near-axis ($\eta \ll 1$) behaviors of this solution for the three inlet flows considered:

case (a):

$$\psi = \frac{B_0 a}{\pi}\eta^2 \ln\eta + A\eta^2 + \mathrm{O}\big(\eta^4 \ln\eta\big), \tag{42}$$

$$\overline{w} = \frac{B_0 a}{\pi}(2\ln\eta + 1) + A + \mathrm{O}\big(\eta^2 \ln\eta\big), \tag{43}$$

$$\overline{v} = \frac{R^2}{\eta} + \frac{B_0 a}{\pi}\eta\ln\eta + A\eta + \mathrm{O}\big(\eta^3 \ln\eta\big), \tag{44}$$

$$\overline{p} = \overline{p_0} + \frac{1}{4\pi^2}\left(2\ln\eta\big(4A\pi^2 R^2 + aB_0 2R^2\pi\ln\eta\big) - \frac{2\pi R^4}{\eta^2}\right) + \mathrm{O}\big(\eta^2 \ln^2\eta\big); \tag{45}$$

case (b):

$$\psi = A\eta^2 + \mathrm{O}\big(\eta^4\big), \tag{46}$$

$$\overline{w} = A + \mathrm{O}\big(\eta^2\big), \tag{47}$$

$$\overline{v} = \frac{A\eta}{1-R^2} + \mathrm{O}\big(\eta^3\big), \tag{48}$$

$$\overline{p} = \overline{p_0} + \frac{A^2\eta^2}{2(1-R^2)^2} + \mathrm{O}\big(\eta^6\big); \tag{49}$$

case (c):

$$\psi = \frac{B_0 a}{\pi}\eta^2 \ln\eta + A\eta^2 + \mathrm{O}\big(\eta^4 \ln\eta\big), \tag{50}$$

$$\overline{w} = \frac{B_0 a}{\pi}\left(\ln\eta + \frac{1}{2}\right) + A + \mathrm{O}\big(\eta^2 \ln\eta\big), \tag{51}$$

$$\overline{v} = R^2\left[\frac{1}{\eta} - \frac{1}{1-R^2}\left(\frac{B_0 a}{\pi}\eta\ln\eta + A\eta\right)\right] + \mathrm{O}\big(\eta^3 \ln\eta\big), \tag{52}$$

$$\overline{p} = \overline{p_0} + \frac{R^4}{4\pi^2(1-R^2)^2}\left[2\ln\eta\big\{-4A\pi^2(1-R^2) - aB_0 2\pi\,(1-R^2)\ln\eta\big\} - \frac{2\pi^2(1-R^2)^2}{\eta^2}\right] + \mathrm{O}\big(\eta^2 \ln^2\eta\big). \tag{53}$$

In the above expressions A is given by

$$A \equiv c_1 + \frac{c_4}{R^2} + \frac{aA_0}{2} + \frac{aB_0}{2\pi}\left(2\gamma - 1 + 2\ln\frac{a}{2}\right), \tag{54}$$

and γ is Euler's constant. The radial velocity component has not been given explicitly because it becomes exponentially small as $\xi \to \infty$. Note that only for the case (b), corresponding to an inlet flow with zero azimuthal velocity at $\eta = \eta_0$ (the inner wall of the pipe does not rotate), all the flow properties are regular at the axis. For the cases (a) and (c), the azimuthal velocity becomes singular at the axis owing to the rotation of the inner body and the conservation of the circulation along streamlines for an inviscid flow and, consequently, all the remaining flow properties are also singular at the axis.

The above asymptotic solution provides a criterion for the breakdown of the inlet flow: in order for the downstream flow to decay exponentially to a cylindrical flow independent of ξ, all the eigenvalues λ_n should be real; otherwise, if any of the λ_n are imaginary, the downstream flow oscillates periodically along ξ. Thus, the condition $\lambda_1 = 0$ provides a maximum value of the swirl parameter, $L = L_f$, above which a cylindrical flow downstream is no longer possible for the given inlet flow. Using (38) and the different definitions of parameter a for the three inlet flows considered, one obtains the following three critical swirl parameters for breakdown:

$$L_f^{(a)} = \frac{j_{1,1}}{2R_p}, \tag{55}$$

$$L_f^{(b)} = \frac{j_{1,1}(1-R^2)}{2R_p} + \mathrm{O}\left(\frac{R_p^2}{R^2}\right), \tag{56}$$

$$L_f^{(c)} = \frac{j_{1,1}(1-R^2)}{2R_p R^2} + \mathrm{O}\left(R_p^4\right) + \mathrm{O}\left(\frac{R_p^4}{R^4}\right). \tag{57}$$

The subsequent conditions $\lambda_n = 0,\ n = 2, 3, \ldots,$ provide other critical values $L = L_{f_n} > L_f$ above which the inviscid flow structure changes again, but they are not so physically relevant as $L_{f_1} \equiv L_f$ because the flow has no longer cylindrical symmetry downstream for $L > L_f$. Note that for a straight pipe without central body ($R = 0,\ R_p = 1$), the critical values for the cases (a) and (b) collapse into $L_f = j_{1,1}/2$, which coincides with the critical value given by Batchelor [9], for a flow rotating as a rigid body inside a straight pipe. Also, this value coincides with that obtained by Chow [10], for a different pipe geometry in the limit of infinite length. In the case (c), $L_f \to \infty$ for a straight pipe with $R = 0$ because the inlet fluid rotation disappears with the inner body (see (10)–(12)).

Another characteristic of the downstream swirling flow is that a near-wall region of flow reversal may be formed above a certain threshold value of the swirl parameter $L = L_r$. To obtain it from the above asymptotic solution one takes into account that the function ψ increases (positive slope) between $\eta_i \leqslant \eta \leqslant \eta_o$ if no flow reversal exists near the outer wall. The onset of near-wall flow reversal requires that the slope of ψ must be zero first, and then negative near the wall. Therefore, the value L_r may be obtained from the condition

$$\frac{\partial \psi}{\partial \eta} = 0 \quad \text{at} \quad \eta = R_p. \tag{58}$$

Using the solution (37) for $\xi \gg 1$,

$$\frac{\partial \psi}{\partial \eta} = -2\eta\left[\left(c_1 + \frac{c_4}{R^2}\right) + aA_0 J_0(a\eta) + aB_0 Y_0(a\eta)\right], \tag{59}$$

so that the condition (58) yields, for the case (a),

$$2L_r^{(a)} R^2 = -2L_r^{(a)}\left(R_p^2 - 1\right) J_0\left(2L_r^{(a)} R_p\right) + 2R_p J_1\left(2L_r^{(a)} R_p\right). \tag{60}$$

Since equation (34) contains no approximation in this case, the resulting $L_r^{(a)}$ from this algebraic equations is exact, valid for any R_p. For R_p small, the values of L_r in the three cases considered are

$$L_r^{(a)} = \frac{\sqrt{2(1-R)}}{R_p} + \frac{1/R - 1}{2\sqrt{2(1-R)}} R_p + \mathrm{O}\left(R_p^3\right), \tag{61}$$

$$L_r^{(b)} = \frac{j_{0,1}(1-R^2)}{2R_p} + \mathrm{O}\left(R_p^2\left(1-R^2\right)\right), \tag{62}$$

$$L_r^{(c)} = \frac{\sqrt{2}(1-R^2)}{R R_p^2} + \mathrm{O}\left(R_p^2\left(1-R^2\right)\right) + \mathrm{O}\left(R_p^5\right), \tag{63}$$

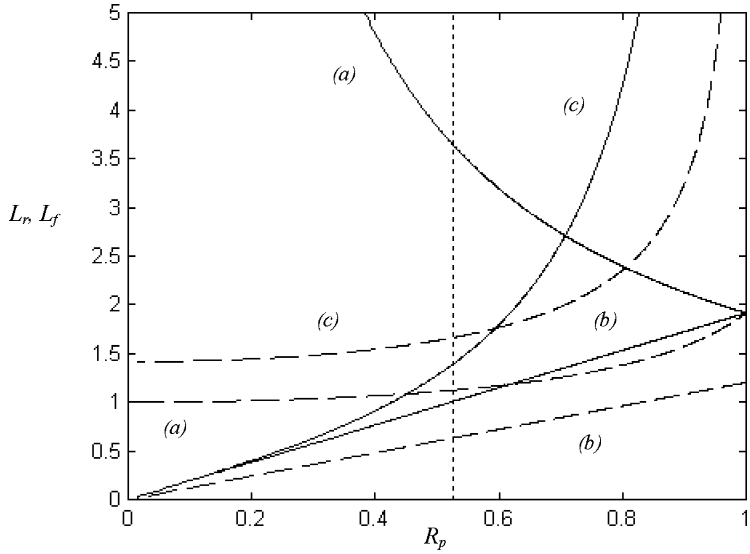

Figure 3. Critical swirl parameters L_f (continuous lines) and L_r (dashed lines) for the three inlet flows considered as functions of $R_p = \sqrt{1-R^2}$. The value $R_p = 0.52678$ used in the numerical computations is marked by a vertical dotted line.

where $j_{0,1}$ is the first zero of the Bessel function J_0. *Figure 3* shows L_f and L_r as functions of R_p in the three cases considered when the fluid section of the pipe is constant ($1 - R^2 = R_p^2$). For the case (a), these functions are valid for any value of R_p (equations (55) and (60)), while in the other two cases they are valid only for small R_p, with errors ranging from $\mathrm{O}(R_p^2)$ to $\mathrm{O}(R_p^4)$ (see (56)–(57) and (62)–(63)). It is interesting to note that for the case (c) $L_r > L_f$ when R_p is small, so that the region of flow reversal near the outer wall appears for a swirl number larger that the critical value for breakdown, after which the present downstream cylindrical solution is no longer valid.

4. Numerical results

To perform the numerical integration of (22)–(29) we shall use a constant value for the interior section $\mathcal{S}(\xi)$ in (7):

$$\mathcal{S}(\xi) = 1 - R^2 \equiv \mathcal{S}_0. \tag{64}$$

It is convenient to transform the fluid domain onto a rectangular one using the new radial co-ordinate

$$\sigma = \frac{\eta_i(\xi) - \eta}{\eta_i(\xi) - \eta_o(\xi)}, \tag{65}$$

so that the computational domain becomes

$$-\xi_1 \leqslant \xi \leqslant \xi_2 \quad \text{and} \quad 0 \leqslant \sigma \leqslant 1. \tag{66}$$

With this transformation, the B–H equation (22) and the boundary conditions (27)–(29) can be written as

$$\psi_{\xi\xi} + f_1\psi_{\xi\sigma} + f_2\psi_{\sigma\sigma} + f_3\psi_\sigma = 4L^2\left[\left\{\sigma(\eta_1 - \eta_0) + \eta_0\right\}^2 \frac{d\overline{H}}{d\psi} - \overline{C}\frac{d\overline{C}}{d\psi}\right], \tag{67}$$

$$\psi(\sigma, \xi = -\xi_1) = \left[\sigma(\eta_1 - \eta_0) + \eta_0\right]^2 - R^2, \quad 0 \leqslant \sigma \leqslant 1, \tag{68}$$

$$\psi(\sigma = 0, \xi) = 0, \quad -\xi_1 \leqslant \xi \leqslant \xi_2, \tag{69}$$

$$\psi(\sigma = 1, \xi) = 1 - R^2, \quad -\xi_1 \leqslant \xi \leqslant \xi_2, \tag{70}$$

$$\psi_{\xi\xi} = 0, \quad \xi = \xi_2,\ 0 \leqslant \sigma \leqslant 1. \tag{71}$$

In (67) the different functions $f_i(\xi, \sigma), i = 1, 2, 3$, are given by:

$$f_1 = 2\eta_i' \frac{1}{\eta_i - \eta_o} - \left[\eta_i' - \eta_o'\right] \frac{2\sigma}{\eta_i - \eta_o}, \tag{72}$$

$$f_2 = \frac{1}{(\eta_i - \eta_o)^2} + \frac{f_1^2}{4}, \tag{73}$$

$$f_3 = \frac{\eta_i''}{\eta_i - \eta_o} - \frac{2[\eta_i' - \eta_o']\eta_i'}{(\eta_i - \eta_o)^2} + \frac{2\sigma[\eta_i' - \eta_o']^2}{(\eta_i - \eta_o)^2} - \frac{\sigma[\eta_i'' - \eta_o'']}{\eta_i - \eta_o} + \left\{\left[\sigma(\eta_i - \eta_o) + \eta_o\right](\eta_i - \eta_o)\right\}^{-1}. \tag{74}$$

To solve the problem (67)–(71) we discretize the derivatives using finite differences in a mesh of $\mathcal{M}$ equidistant points along the σ-direction, and $\mathcal{N}$ points in the ξ-direction, resulting a system of $\mathcal{M} \times \mathcal{N}$ non-linear algebraic equations for the unknowns ψ_k on each node $k = (m, n),\ 1 \leqslant m \leqslant \mathcal{M},\ 1 \leqslant n \leqslant \mathcal{N}$. This system can be written formally as

$$F(\psi; \lambda) \equiv 0, \tag{75}$$

where λ represents the different parameters of the problem and F is the matrix operator resulting from the discretization. Equation (75) can be solved iteratively using Newton's method. One iteration of this method consists of solving the linear system of equations

$$F_\psi(\psi^i; \lambda)\delta\psi = -F(\psi^i; \lambda), \tag{76}$$

$$\psi^{i+1} = \psi^i + \delta\psi, \tag{77}$$

where F_ψ is the Jacobian matrix (the (j, k) element of this matrix is $F_{\psi_{j,k}} = \partial F_j/\partial\psi_k$ for $1 \leqslant j \leqslant \mathcal{M} \times \mathcal{N},\ 1 \leqslant k \leqslant \mathcal{M} \times \mathcal{N}$). If a good initial guess ψ^0 is used, the successive application of this iteration will result in the converging of ψ^i to the final solution ψ. In all the three cases we used the inlet flow as the initial guess, which makes fastest the convergence of the method. Typically a solution can be found in a few iterations since the convergence of the method is quadratic (in the case (a) the system is linear and only one iteration is needed to reach the final solution). The values ξ_1 and ξ_2 have to be chosen large enough for the inner and outer walls of the pipe be parallel to the axis of symmetry at the inlet and outlet regions. As shown in *figure 1*, these values have to be increased (particularly ξ_1) as α decreases. To be sure that the pipe wall is straight both at the inlet and at the outlet for a variety of values of α, we have used $\xi_1 = 10$ and $\xi_2 = 10$ in all the computations. Also, we fixed $R = 0.85$ and $R_p = \sqrt{1 - R^2} = 0.526783$ (see *figure 3* for the corresponding asymptotic values of L_r and L_f in the three cases). With this geometry, a grid of 300×200 points was enough to reach a precision of at least four digits in all the reported results. To illustrate the convergence of the method, we plot in *figure 4* the radial profile of the streamfunction just after the central body base, where the radial gradient is the largest, for 3 different grids. Only the profile for the grid 200×200 is slightly different in a thin region near the maximum of ψ (see the detail in *figure 4(b)*), while for the other two grids the profiles practically collapse.

First of all we consider the case in which the geometric parameter α is unity. *Figure 5* shows, for the three inlet flows (a), (b) and (c), the streamlines obtained numerically for a value of L smaller than L_r. Note that a near-axis region of flow reversal is formed in the case (c). This flow configuration occurs even for negligible swirl ($L \to 0$). For L larger than $L_r < L_f$, a region of flow reversal is formed near the outer wall, as is seen

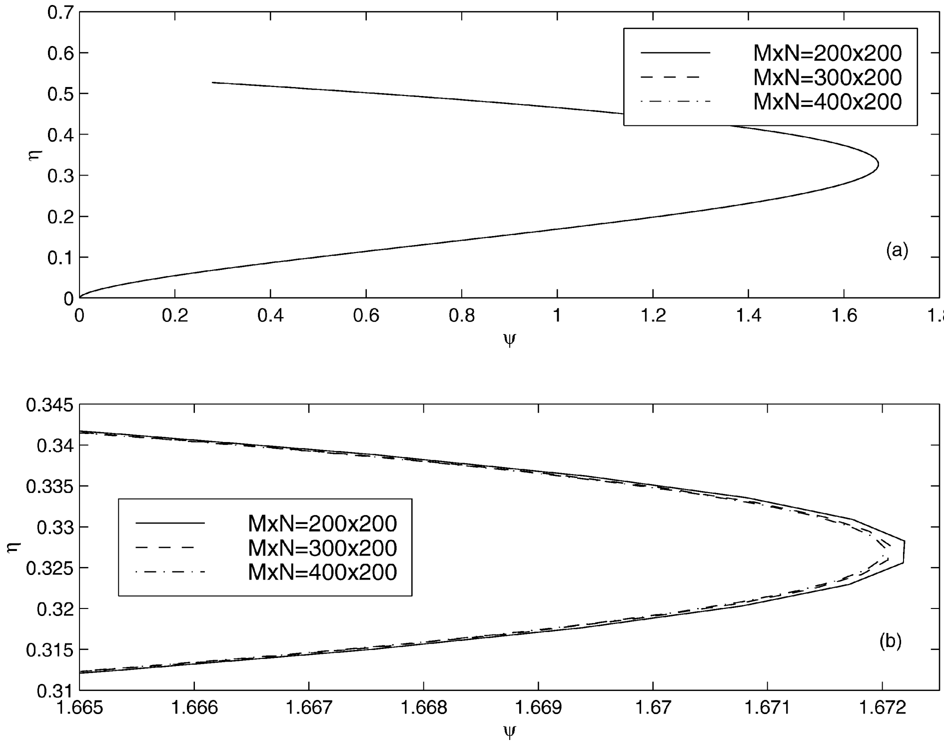

Figure 4. Streamfunction radial profiles $\psi(\eta)$ for the case (a) and $L = 3$ just after the central body base ($\xi = 0.05025$) for the three different grids indicated. In (a) it is plotted the whole profile for $0 \leqslant \eta \leqslant R_p$, while in (b) it is shown a detail near the maximum of ψ.

in *figure 6* (except for the case (c), where $L_r > L_f$ and the solution is not shown here). Finally, when L is larger than L_f, the flow structure changes dramatically, appearing a periodic flow with many bubbles with flow recirculation, as it is seen in *figure 7* for the case (a) (for the other two inlet flows the iterative method does not converge when $L > L_f$). Clearly, the flow has no longer a cylindrical structure downstream, as already predicted by the asymptotic analysis of the previous section. New changes in the flow pattern are observed when L increases above the successive critical values L_{f_n}, given approximately by the asymptotic solution of the last section (see Chow [10] for qualitatively similar results in a different pipe geometry).

Figures 8 to *10* compare the asymptotic solution given in the previous section with the numerical results. In particular, *figure 8* shows the radial variation of the stream function at the pipe outlet ($\xi = \xi_2 = 10$) for $L < L_r$, *figure 9* for $L > L_r$ (only the cases (a) and (b)), and *figure 10* for $L > L_f$ (only the case (a)). As expected, the agreement is excellent near the axis (small η), but becomes poorer as the outer wall is reached (note that the selected value $R_p = 0.526783$ for the outlet radius of the pipe is not so small).

In order to better appreciate the transformations in the downstream flow structure as L increases, *figure 11* shows the axial velocity $\overline{w}$ at the pipe outlet obtained numerically for different values of L corresponding to an inlet flow (a). It is observed that without rotation, $L = 0$, the axial velocity is uniform across the outlet section (its value is unity from continuity). When a rotation is introduced into the flow, the axial velocity becomes singular at the axis, even for very small values of L. The effect of increasing L until $L = L_f$ is to accelerate the flow near the axis of symmetry, and decelerate it at the outer wall, being zero there when $L = L_r$, and becoming negative for $L_r < L \leqslant L_f$.

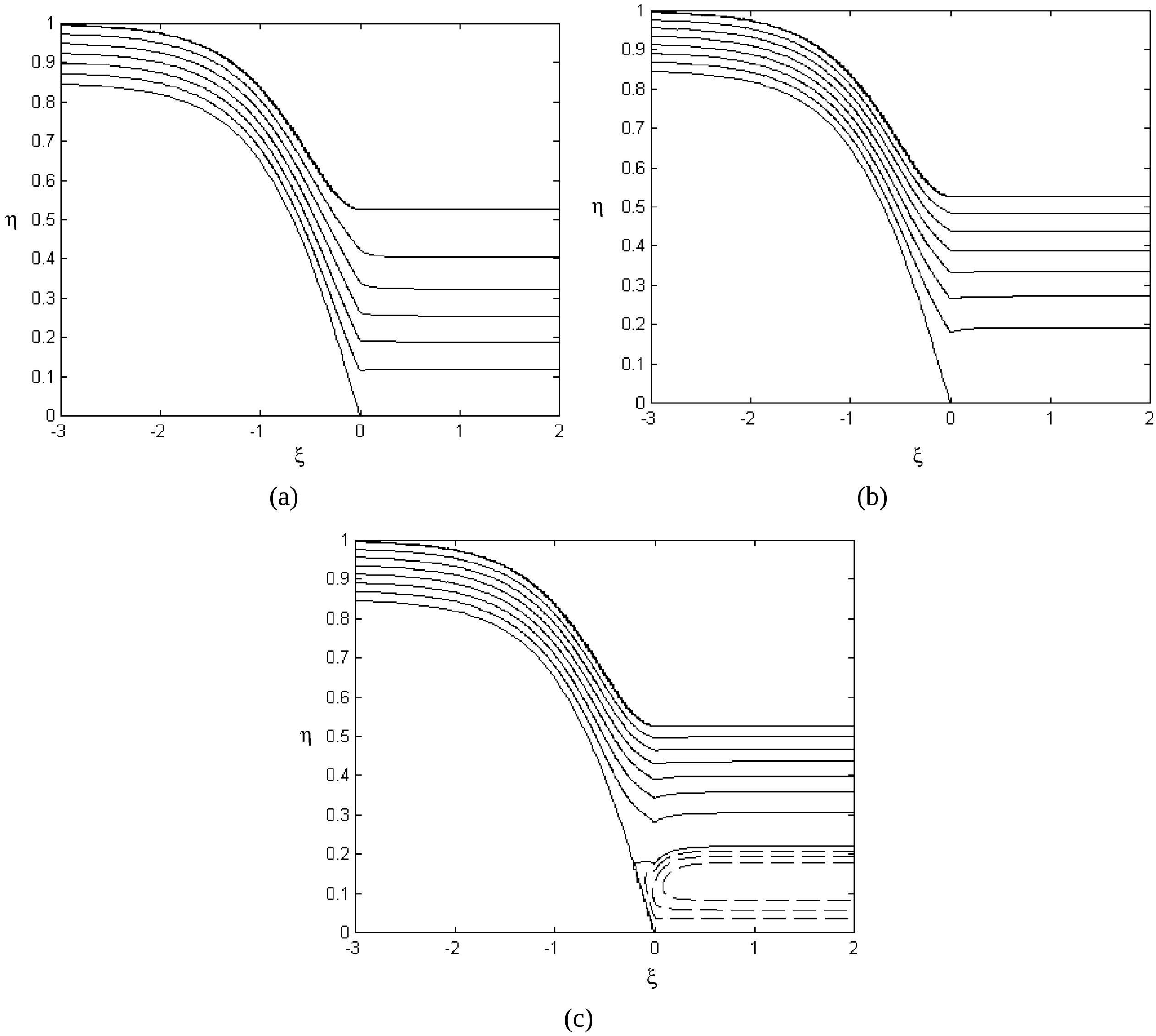

Figure 5. Streamlines when $L < L_r$ for the three inlet flows considered. (a) $L = 1$, (b) $L = 0.25$, and (c) $L = 0.8$. Dashed lines correspond to $\psi < 0$.

We have seen that, for the third type of inlet flow considered (c), a zone of flow reversal is always present near the axis for $L > 0$, with the streamline $\psi = 0$ starting at some point in the central body wall (see *figure 5(c)*). It would be of interest to know whether this axial 'bubble' with flow recirculation can be separated form the inner wall by changing the pipe geometry, for instance by introducing a pipe expansion in the downstream flow section just after the central body base. To that end we have considered a different interior section $\mathcal{S}(\xi)$ of the pipe with a contraction-expansion region between two given axial locations ξ_a and ξ_b:

$$\mathcal{S}(\xi) = \mathcal{S}_0 = 1 - R^2 \quad \text{for } -\xi_1 \leqslant \xi \leqslant \xi_a, \tag{78}$$

$$\mathcal{S}(\xi) = \mathcal{S}_0 + \frac{1}{2}\alpha_c\left(\cos\left(2\pi\frac{\xi - \xi_a}{\xi_b - \xi_a}\right) - 1\right) \quad \text{for } \xi_a < \xi \leqslant \xi_b, \tag{79}$$

$$\mathcal{S}(\xi) = \mathcal{S}_0 \quad \text{for } \xi_b < \xi \leqslant \xi_2. \tag{80}$$

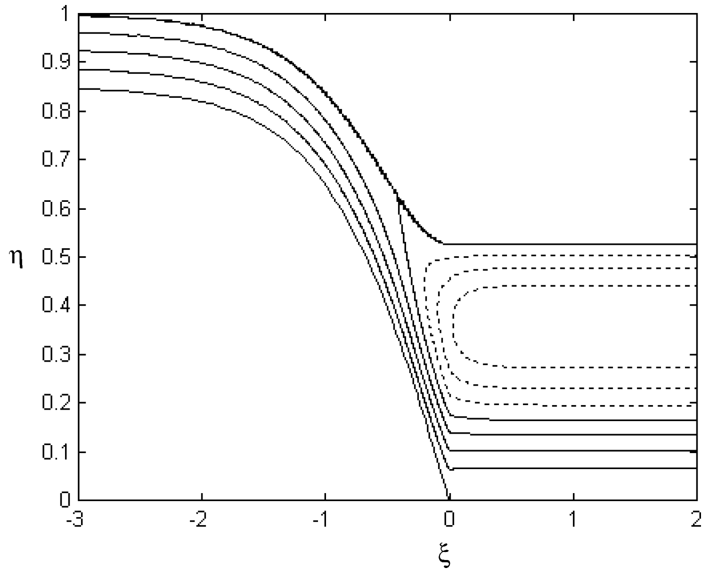

(a)

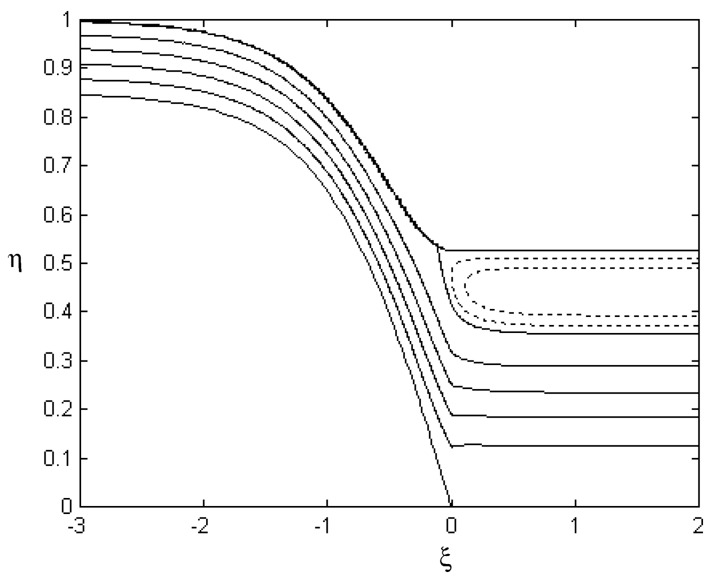

(b)

Figure 6. Streamlines when $L_r < L < L_f$ for the cases (a) $L = 2$ and (b) $L = 0.8$. Dotted lines correspond to $\psi > (1 - R^2)$.

The pipe interior has thus a minimum section $\mathcal{S}_0 - \alpha_c$ located at $\xi_m = (\xi_b + \xi_a)/2$. We have tried different values of ξ_a, ξ_b and α_c, and found that for a contraction–expansion centered at $\xi_m = 0$ (e.g. $\xi_a = -2$ and $\xi_b = +2$), there exists for each L a contraction factor $\alpha_c^*(L)$ above which the $\psi = 0$ streamline becomes detached from the inner body. For $\alpha_c > \alpha_c^*(L)$ a stagnation point is thus formed at some location in the axis, and a open bubble of flow reversal is formed after it (see *figure 12*).

Finally, we have also considered the influence of the axial characteristic length of the pipe α. *Figure 13* shows the streamlines corresponding to $\alpha = 2$ for an inlet flow of type (a) with three different values of L. It is

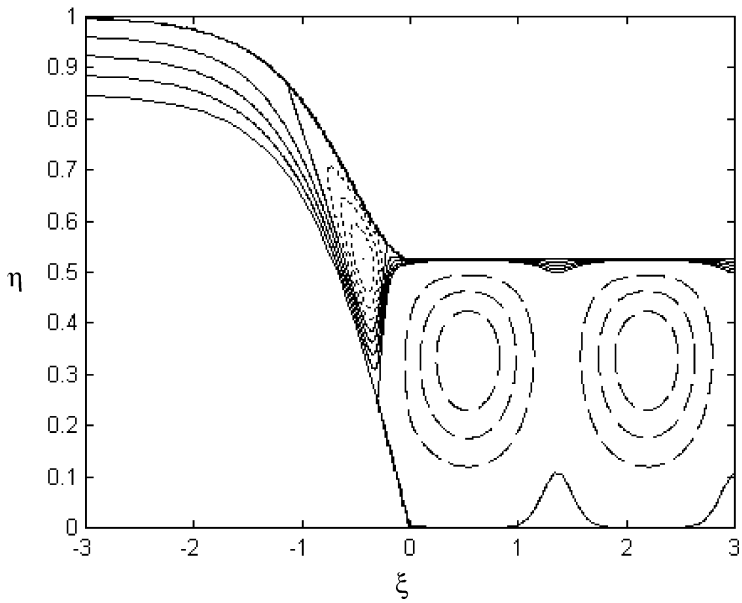

Figure 7. Streamlines for the case (a) when $L = 4.1 > L_f^{(a)}$. Dashed lines correspond to $\psi < 0$ and dotted lines to $\psi > (1 - R^2)$.

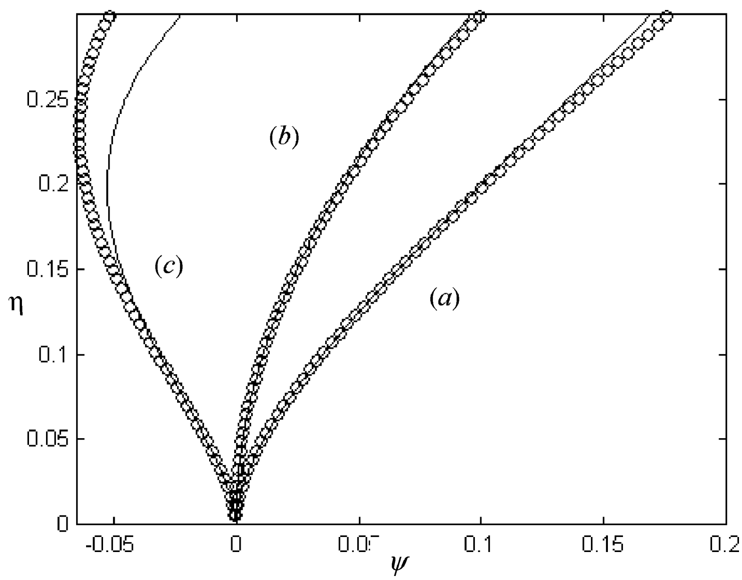

Figure 8. Streamfunction $\psi(\eta)$ at the pipe outlet ($\xi = 10$) obtained numerically (continuous lines) and asymptotically (circles) for the three inlet flows considered with $L < L_r$: (a) $L = 1$, (b) $L = 0.25$, and (c) $L = 0.8$.

observed that, in relation to the pipe with $\alpha = 1$, only minor changes are produced in the flow near the region where the central body ends. Far downstream the flow is, as predicted by the asymptotic analysis, independent of α (see *figure 14*, where the outlet ($\xi = \xi_2$) axial velocity profiles for $\alpha = 1$ and $\alpha = 2$ are compared).

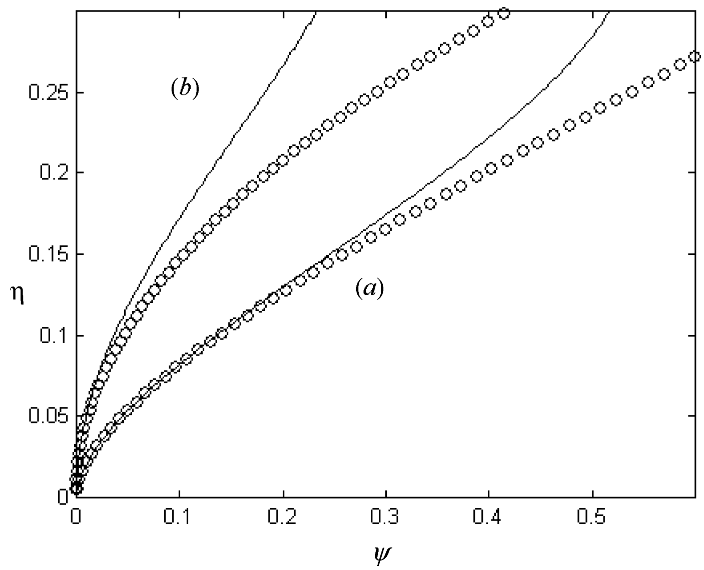

Figure 9. As *figure 8*, but for $L > L_r$ in cases (a) $(L = 2)$ and (b) $(L = 0.8)$.

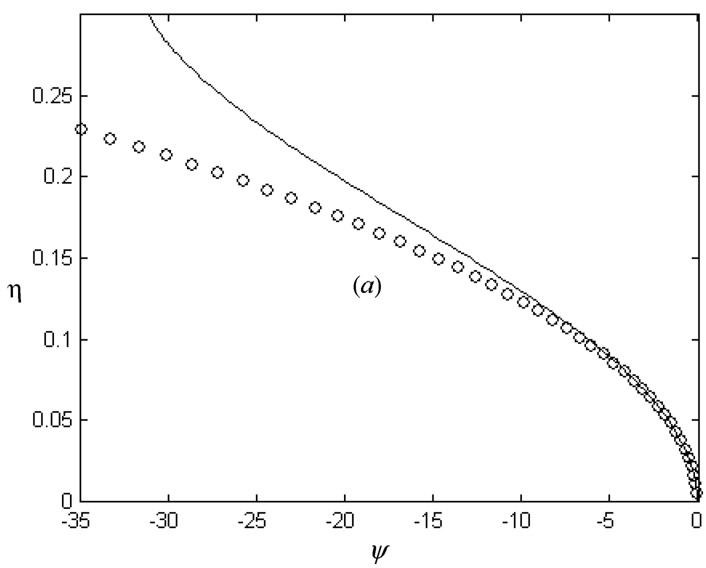

Figure 10. As *figure 8*, but $L = 3.7 > L_f$ and only for an inlet flow of type (a). Note that in this case $\psi < 0$ and its absolute value is much larger than the previous cases owing to the bubble structure of the downstream flow.

5. Conclusions and discussion

We have analyzed the influence of the inlet flow on the inviscid evolution of an incompressible swirling flow in a pipe with a central body inside, an element present in most swirl generators, which usually concentrates the swirl at the axis of the pipe. Three different inlet flows have been considered far upstream. These inlet flows yield genuine inviscid velocity profiles at the entrance of the straight section of the pipe just after the central body base. Two of these entrance flows are singular at the axis of symmetry, corresponding to a rotation of the central body, with and without rotation of the outer wall upstream (cases (a) and (c)), and the other one

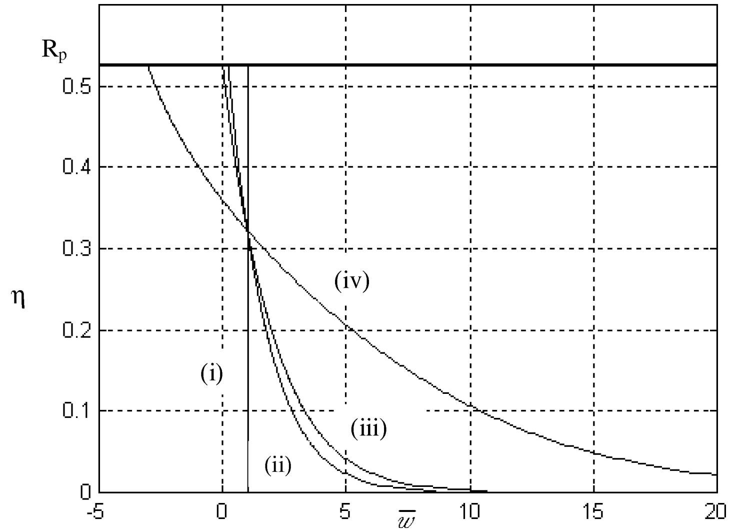

Figure 11. Axial velocity profiles at the pipe outlet ($\xi = 10$) for (i) $L = 0$, (ii) $L = 1 < L_r$, (iii) $L = L_r \approx 1.1246$, and (iv) $L = 2 > L_r$, in the case of an inlet flow of type (a).

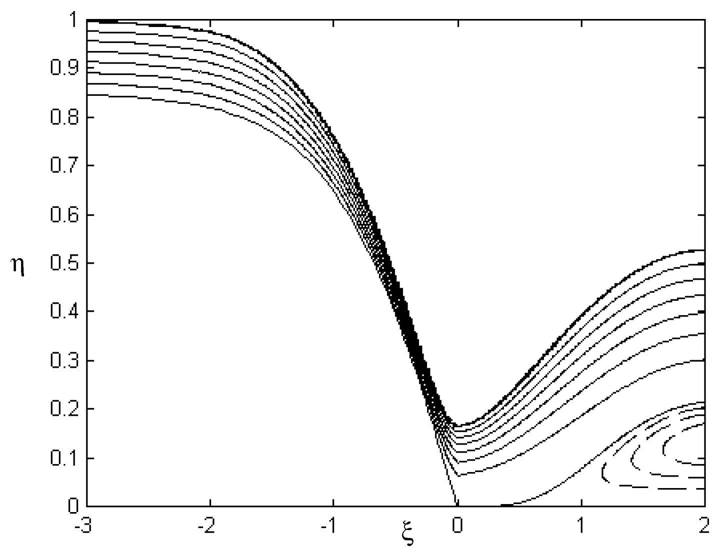

Figure 12. Streamlines for the same case plotted in *figure 5(c)* but with a contraction–expansion region in the pipe centered at $\xi_m = 0$, with $\xi_a = -2$, $\xi_b = 2$, and $\alpha_c = 0.25$. Dashed lines correspond to $\psi < 0$.

is regular at the axis, corresponding to a rotation of the outer wall with the central body at rest (case (b)). Asymptotic and numerical solutions to the Bragg–Hawthorne equation governing the inviscid evolution of the axisymmetric swirling flow show that the structure of the downstream flow changes when the inlet swirl parameter L passes two different threshold values, which depend on the pipe geometry and on the inlet flow. It is shown that dependence on the inlet velocity profile is not just quantitative, but qualitative. In particular, the value L_f above which the far downstream flow has no longer cylindrical symmetry (vortex breakdown) depends strongly on the inlet flow considered. The inlet flow corresponding to a central body rotation with the outer pipe wall at rest (case (c)) is of particular interest because the inviscid evolution of the flow predicts that a

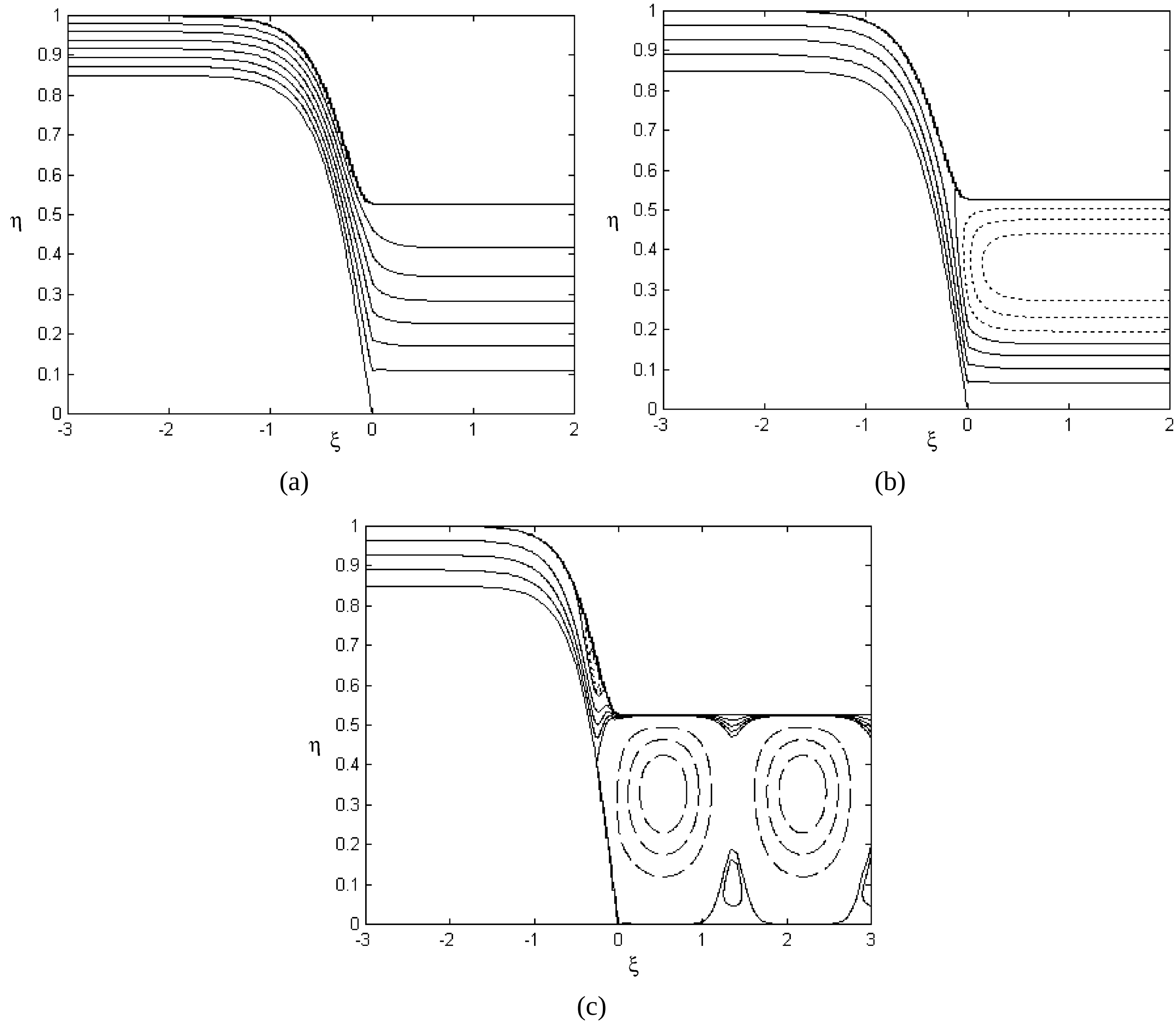

Figure 13. Streamlines for an inlet flow of type (a) with $\alpha = 2$. (a) $L = 1$, as in *figure 5(a)*, (b) $L = 2$, as in *figure 6(a)*, and (c) $L = 4.1$, as in *figure 7*. Dashed lines correspond to $\psi < 0$ and dotted lines to $\psi > (1 - R^2)$.

near-axis region with flow reversal is always present downstream, even for vanishing inlet swirl. Also, for this case, the value of L_r above which a zone of flow reversal near the outer wall is formed downstream is larger than L_f, so that, contrary to the other two cases, this flow configuration is never reached. In the other two cases considered, $L_r < L_f$, so that, as L increases, a region of flow reversal near the outer wall is always formed before the axial swirling flows breaks down. All these results show that one has to be cautious before drawing conclusions about the behavior (particularly breakdown) of swirling flows in pipes from the inviscid equations alone.

Finally, it must be stressed here that we have only considered the effect of three different circumferential velocity profiles at the pipe inlet on the downstream evolution of the inviscid flow according to the B–H equations. Although these profiles correspond to three realistic combinations of upstream pipe rotation, we

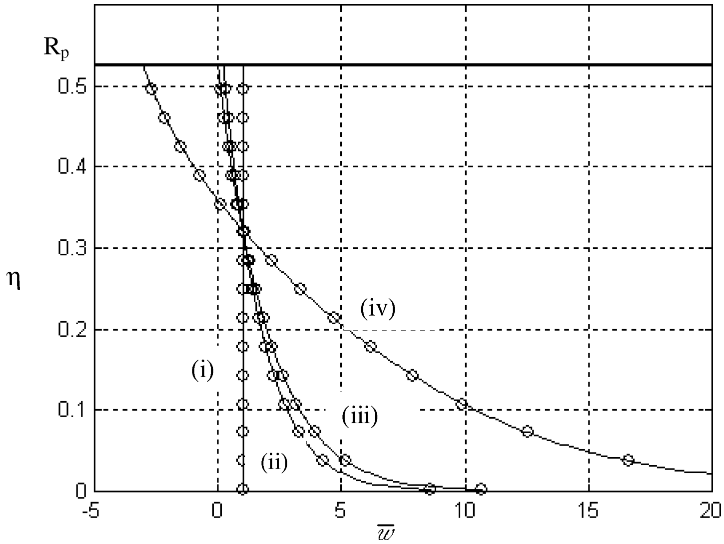

Figure 14. Comparison between the outlet axial velocity profiles ($\xi = 10$) for an inlet flow of type (a) when $\alpha = 1$ (lines) and $\alpha = 2$ (circles), for the same values of L of *figure 11*.

have not considered the effect of viscosity on the inlet axial velocity profiles (thin boundary layers on the pipe walls), to be consistent with a purely inviscid analysis. The evolution of these boundary layer may modify in a significant way the downstream flows found here, especially when separation occurs at the pipe wall or at the axis. In fact, although we have found that separation may occur even when no boundary layers are taken into account, the inviscid flow inside the regions of recirculating flow for $L > L_r$ or $L > L_f$ (near the wall or at the axis) are not uniquely specified within the present analysis because the functions H and C are not defined when the streamlines are not connected to the inlet. In addition, viscosity is essential to describe the flow near the separating streamlines, connecting separated regions to the main flow in a realistic way. However, these viscous analyses are out of the scope of this paper. What we show here is that swirling flows in pipes are very sensitive to the way in which the swirl originates upstream even when viscosity is wholly neglected.

Acknowledgements

This work has been supported by the Ministerio de Educación y Cultura of Spain, Grant number PB96-0679-C02-01, and by a NATO Collaborative Research Grant, CRG 950368.

References

[1] Delery J.M., Aspects of vortex breakdown, in: Young A.D. (Ed.), Progress in Aerospace Sciences 30 (1994) 1–59.
[2] Sarpkaya T., On stationary and traveling vortex breakdowns, J. Fluid Mech. 45 (1971) 545–559.
[3] Beran P.S., Culik F.E.C., The role of non-uniqueness in the development of vortex breakdown in tubes, J. Fluid Mech. 242 (1992) 491–527.
[4] Stuart J.T., A critical review of vortex-breakdown theory, in: Proc. 2nd Int. Colloq. Vortical Flows, Baden, Swizerland, 1987, pp. 131–153.
[5] Buntine J.D., Saffman P.G., Inviscid swirling flows and vortex breakdown, P. Roy. Soc. Lond. A 449 (1995)139–153.
[6] Wang S., Rusak Z., The dynamics of swirling flows in a pipe and transition to axisymmetric vortex breakdown, J. Fluid Mech. 340 (1997) 177–223.
[7] Bragg S.L., Hawthorne W.R., Some exact solutions of the flow through annular cascade actuator discs, J. Aero. Sci. 17 (1950) 243–249.
[8] Abramowitz M., Stegun I.A. (Eds), Handbook of Mathematical Functions, Dover, New York, 1964, Chapter 9.
[9] Batchelor G.K., An Introduction to Fluid Dynamics, Cambridge University Press, 1967, Section 7.5.
[10] Chow C.Y., Swirling flows in tubes of non-uniform cross-sections, J. Fluid Mech. 38 (1969) 843–854.